Van der Waals-Like Isotherms in a Confined Electrolyte by Spherical and Cylindrical Nanopores

4 AUTHORS, INCLUDING:

Gabriel Eloy Aguilar-Pineda
Autonomous University of Mexico City
5 PUBLICATIONS   25 CITATIONS

SEE PROFILE

Felipe Jimenez-Angeles
Reservoir Engineering Research Institute
34 PUBLICATIONS   368 CITATIONS

SEE PROFILE

Marcelo Lozada-Cassou
Universidad Nacional Autónoma de México
118 PUBLICATIONS   2,474 CITATIONS

SEE PROFILE

Van der Waals-Like Isotherms in a Confined Electrolyte by Spherical and Cylindrical Nanopores

Gabriel E. Aguilar-Pineda,[†,‡] **Felipe Jiménez-Ángeles,**[§] **Jiang Yu,**[†] **and Marcelo Lozada-Cassou*,**[§]

Departamento de Física, Universidad Autónoma Metropolitana-Iztapalapa Apartado Postal 55-534, 09340 México, D. F., México, Colegio de Ciencia y Tecnología, Universidad Autónoma de la Ciudad de México, Fray Servando Teresa de Mier 99, 06080, México, D. F., México, and Programa de Ingeniería Molecular, Instituto Mexicano del Petróleo, Lázaro Cárdenas 152, 07730 México, D. F., México

Electrolytes confined by spherical, cylindrical, and slit-like charged nanopores are studied. Results for ionic distribution profiles, pressures of the confined fluid, and absorption isotherms are obtained through the hypernetted chain/mean spherical approximation (HNC/MSA) integral equations theory. In spherical and cylindrical geometries, an inward, non-monotonic behavior of the pressure is found as confinement increases, implying a negative compressibility. The pressure vs volume isotherms resemble liquid−vapor van der Waals-like phase transition diagrams. This effect is correlated with a charge separation inside a spherical pore previously reported (*Phys. Rev. Lett.*, **79,** *3656*, 1997). Here, the mechanism of charge separation and negative compressibility are explored in detail. When compared with the slit-like pore pressure, important qualitative differences are found.

I. Introduction

Fluids subject to *high* confinement appear in many systems of disciplines ranging from biophysics to material science.[1−5] Some examples of confining cavities are nanotubes, the molecular channels formed by some membrane proteins, and micelles, among many others.[6−11] The term high confinement refers to a fluid inside a cavity with at least one of its dimensions in the range of 10^{-10} to 10^{-8} m. Due to the small size of of these cavities (like micelles) only a few tens of particles can be allocated inside of, for example, a spherical cavity. In the case of nanotubes or slits, the number of confined molecules is very high; however, in at least one dimension, they are packed in just a few layers. It is the confinement of a fluid that produces a broad variety of interesting phenomena.[12−19] For example, nanometric slit cavities may induce phase transitions of confined water, above its freezing temperature and atmospheric pressure, which occur only under high slit confinement.[20−22]

Previously, a model for a charged spherical cavity immersed in an electrolyte solution was studied.[12] In this simple system, it was found that the electrolyte inside the spherical cavity is separated in two "phases": coions are segregated toward the central region, whereas counterions form a spherical shell around a coion core. Furthermore, the pressure isotherms as a function of the pore size closely resemble the van der Waals (VW) liquid−vapor phase transition (LVPT) curves; i.e., they exhibit maximum and minimum loops. The prerequisites for these phenomena to occur are the high confinement and the constant chemical potential between the confined and unconfined fluids. In the VW−LVPT, the pressure prediction inside the spinodal curve is unphysical, because it implies a negative compressibility. However, in our case, due to the confinement of charged walls, the pressure loops are real. This atypical behavior has

been experimentally observed,[2] and the theoretical prediction was also corroborated by MC simulations.[12] Recent studies have reported this van der Waals-like behavior for a variety of confined systems.[23−25] When compared with the slit pore, the spherical nanopore pressure is totally different. In this paper, we will study the pressure behavior, as a function of the pore size, for spherical, cylindrical, and slit-like geometries.

Charge separation is related with two effects previously reported: violation of the local electroneutrality condition (VLEC) and fluid−fluid correlation across the charged wall.[26,27] These phenomena in turn imply that two fluids separated by a charged wall do not necessarily compensate the charge of the corresponding surface with which they are in contact; however, both fluids necessarily compensate the total wall's charge, satisfying the overall electroneutrality condition.

Studies of confined RPM electrolytes have been previously carried out by means of computer simulations, density functional, and integral equation theories.[28−32] This model has been helpful in understanding a broad variety of phenomena, such as VLEC, fluid−fluid correlation across permeable and semipermeable walls, charge reversal, charge inversion, and overcharging.[33−37] In the RPM, the ions are considered as hard spheres, with a point charge localized in their centers; the solvent is taken as a continuous medium with dielectric constant ϵ. The inclusion of nonelectrostatic short range interactions of the ions is an important factor for determining the structure and the thermodynamics properties of the confined fluid.

One manner to study confined fluids is by means of integral equations theories for inhomogeneous fluids based on the Ornstein−Zernike equation. A particularly successful integral equations theory is the hypernetted chain-mean spherical approximation (HNC/MSA). In the case of nonuniform electrolytes, reduced concentration profile results from HNC/MSA have shown good agreement with density functional theories and computer simulations in planar,[38−41] spherical,[42,43] and cylindrical[35,44] geometries. HNC/MSA pressure calculations of

† Departamento de Física.
‡ Colegio de Ciencia y Tecnología.
§ Programa de Ingeniería Molecular.

confined charged fluids have been compared with Monte Carlo (MC) computer simulations and with experimental results: the HNC/MSA pressure for electrolytes confined between two plates[26] and by a spherical nanopore[12] exhibits good agreement with MC results. On the other hand, HNC/MSA osmotic pressure calculations for a model macroion solution confined by a semipermeable membrane are also in good agreement with experimental results.[36] In the same way, as compared with computer simulation results, HNC/MSA has shown to predict properly the behavior of the surface and Helmholtz potentials,[35,43,45] the violation of local electroneutrality condition,[26] the correlation between two fluids separated by a wall,[46] and charge reversal[35,42] to mention some. This evidence implies that HNC/MSA reasonably accounts for many body correlations in a broad variety of instances.

In this paper, we solved the HNC/MSA integral equations for a RPM electrolyte confined by a charged nanopore of (i) spherical, (ii) cylindrical, and (iii) slit-like geometries. The pressure on the pore's walls, $p(R)$, defined as the pressure inside the pore, p_0, minus the pressure outside, p_{bulk}, as a function of the pore radius, R, is analyzed for a broad variety of conditions. Important phenomena such as charge separation, inward pressure, and anomalous compressibility behavior, attributed to the confined geometry, are discussed, and an explanation is offered. The paper is organized as follows. Section II provides a theoretical description of the spherical, cylindrical, and slit-like nanopores. The HNC/MSA equations are also derived in the same section. In Section III, results for the pressure, $p(R)$, for the reduced concentration profiles and the absorption isotherms are discussed for a variety of conditions. Finally, some conclusions are given in Section IV.

II. Theory

A. Integral Equations for Confined Fluids. The method that we use to study confined fluids is based on the multicomponent Ornstein−Zernike equation, where the total correlation function, $h_{ij}(\mathbf{r}_{21}) \equiv g_{ij}(\mathbf{r}_{21}) - 1$, between two particles of species i and j is given by

$$h_{ij}(\mathbf{r}_{21}) = c_{ij}(\mathbf{r}_{21}) + \sum_{m=1}^{n} \rho_m \int h_{im}(\mathbf{r}_{23}) c_{mj}(\mathbf{r}_{13})\, d\mathbf{r}_3 \quad (1)$$

where $c_{ij}(\mathbf{r}_{21})$ is the direct correlation function, ρ_m is the concentration of species m, $\mathbf{r}_{21} \equiv \mathbf{r}_1 - \mathbf{r}_2$ is the relative position between particles 1 and 2, and n is the number of species in the fluid.

The equivalence between particles and fields implies that one can consider an external field as another particle, and in the same manner, a particle can be considered just like an external field. If we apply this concept into the Ornstein−Zernike equation, we can assume that the charged nanopore is just another particle in the fluid, which is assigned to be the $n + 1$ species and referred to as the α species, which is at infinite dilution; i.e., $\rho_\alpha \rightarrow 0$. Therefore, the total correlation between the electrolyte and the charged nanopore is

$$h_{\alpha j}(\mathbf{r}_{21}) = c_{\alpha j}(\mathbf{r}_{21}) + \sum_{m=1}^{n} \rho_m \int h_{\alpha m}(\mathbf{r}_{23}) c_{mj}(\mathbf{r}_{13})\, d\mathbf{r}_3 \quad (2)$$

Notice that the summation in the second term at the right-hand side of eq 2 runs up to n, meaning that the α species is not included in the summation. In this paper we use the HNC closure for $c_{\alpha j}(\mathbf{r}_{21})$, which is given by

$$c_{\alpha j}(\mathbf{r}_{21}) = h_{\alpha j}(\mathbf{r}_{21}) - \ln[g_{\alpha j}(\mathbf{r}_{21})] - \beta u_{\alpha j}(\mathbf{r}_{21}) \quad (3)$$
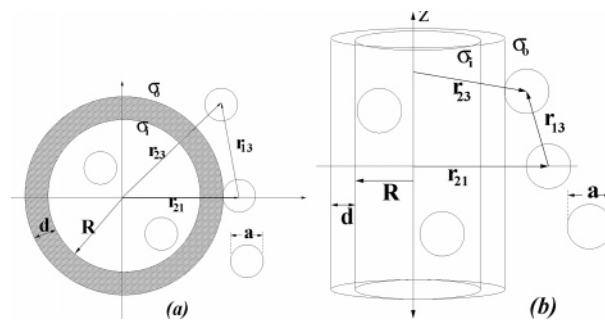

Figure 1. Schematic representation of the models setup: (a) the spherical shell and (b) the cylindrical pore.

where $u_{\alpha j}(\mathbf{r}_{21})$ is the direct interaction potential between species α and j. Substituting this equation in eq 2 we obtain

$$g_{\alpha j}(\mathbf{r}_{21}) = \exp\{-\beta u_{\alpha j}(\mathbf{r}_{21}) + \sum_{m=1}^{n} \rho_m \int h_{\alpha m}(\mathbf{r}_{23}) c_{mj}(\mathbf{r}_{13})\, d\mathbf{r}_3\} \quad (4)$$

In our treatment, we assume that the direct correlation function, $c_{mj}(\mathbf{r}_{13})$, is that for a *homogeneous* bulk fluid, which can be obtained independently of eq 2. In particular, we have used the MSA, which is given by

$$c_{ij}(\mathbf{r}_{13}) = -\beta u_{ij}(\mathbf{r}_{13}) \qquad |\mathbf{r}_{13}| > a \quad (5)$$

where $u_{ij}(\mathbf{r}_{13})$ is the direct interaction potential between two particles in the bulk fluid of species i and j with their closest approach distance a and $\beta = 1/k_B T$ (where k_B is the Boltzmann constant and T is the absolute temperature). The advantage of using eq 5 in the Ornstein−Zernike equation for homogeneous fluids is that in many cases it produces an analytic expression for $c_{ij}(\mathbf{r}_{13})$ for $|\mathbf{r}_{13}| \leq a$. This manner of deriving integral equation theories for inhomogeneous fluids is known as the Direct Method,[47,48] and it has been employed to study many cases of confined and inhomogeneous fluids.

B. Models. We consider a two component restricted primitive model (RPM) electrolyte. The two fluid species are taken as charged hard spheres of diameter a bearing a centered point charge $q_i = z_i e$, where z_i is the ionic valence, e is the proton's charge, and $i = +$ or $-$ (+ for cations and − for anions). The particles are embedded in a uniform medium of dielectric constant ϵ; therefore, their interaction potential energy is given by

$$u_{ij}(r) = \begin{cases} \infty & r < a \\ \dfrac{z_i z_j e^2}{\epsilon r} & r \geq a \end{cases} \quad (6)$$

Within this electrolyte, there is immersed a nanopore considered of (i) spherical or (ii) cylindrical geometry, and the electrolyte is allowed to permeate inside of the nanopore in such a way that the inner and outer fluids are at constant chemical potential. The nanopore has an inner radius R and a wall thickness d, and its inner and outer surfaces carry a uniform surface charge density σ_i and σ_o, respectively. The dielectric constant of the nanopore is taken to be ϵ so that no image forces are present. We refer the reader to Figure 1a for the spherical setup and Figure 1b for the cylindrical one.

In the MSA applied to the RPM electrolyte, the direct correlation function between two ions of species m and j, $c_{mj}(\mathbf{r}_{13})$, depends only on their relative distance, $r_{13} \equiv |\mathbf{r}_{13}|$, and

Van der Waals-like Isotherms in Confined Electrolyte

J. Phys. Chem. B, Vol. 111, No. 8, 2007 **2035**

has an analytical expression, which is written as

$$c_{mj}(r_{13}) = c^{hs}(r_{13}) + q_m q_j c^{sr}(r_{13}) - \frac{\beta q_m q_j}{\epsilon r_{13}} \qquad (7)$$

where $c^{hs}(r_{13})$ and $c^{sr}(r_{13})$ are equal to zero for $r_{13} > a$, and[49,50]

$$c^{hs}(r_{13}) = -c_1 - 6\eta c_2 r_{13} - \frac{1}{2}\eta c_3 r_{13} \qquad (8)$$

and

$$c^{sr}(r_{13}) = \frac{\beta}{\epsilon}\left[\frac{1}{r_{13}} - \frac{2\Gamma}{1+\Gamma a} + \frac{\Gamma^2}{(1+\Gamma a)^2}r_{13}\right] \qquad (9)$$

for $r_{13} \leq a$.

The constants in these expressions are given by

$$\eta = \frac{1}{6}\pi a^3 \sum_{m=1}^{n} \rho_m \qquad (10)$$

$$c_1 = \frac{(1+2\eta)^2}{(1-\eta)^4} \qquad (11)$$

$$c_2 = -\frac{(1+0.5\eta)^2}{a(1-\eta)^4} \qquad (12)$$

$$c_3 = \frac{c_1}{a^3} \qquad (13)$$

$$\Gamma a = -\frac{1}{2} + \frac{1}{2}\sqrt{1+2\kappa a} \qquad (14)$$

$$\kappa^2 = \frac{4\pi\beta e^2}{\epsilon}\sum_{m=1}^{n}\rho_m z_m^2 \qquad (15)$$

Substituting eq 7 into eq 4 we have

$$g_{\alpha j}(\mathbf{r}_{21}) = \exp\left\{-\beta u_{\alpha j}(\mathbf{r}_{21}) + \sum_{m=1}^{2}\rho_m\int h_{\alpha m}(\mathbf{r}_{23})\frac{q_m q_j}{\epsilon r_{13}}\,d\mathbf{r}_3 + \right.$$
$$\left. \sum_{m=1}^{2}\rho_m\int h_{\alpha m}(\mathbf{r}_{23})[c^{hs}(r_{13}) + q_m q_j c^{sr}(r_{13})]\,d\mathbf{r}_3\right\} \qquad (16)$$

Because we have used a hybrid closure to derive this equation, i.e., MSA for $c_{mj}(\mathbf{r}_{13})$ and HNC closure for $c_{\alpha j}(\mathbf{r}_{21})$, eq 16 is referred to as the HNC/MSA equation. The boundary conditions, such as the geometry of confinement and the information of the external field, should be included in the expression for $u_{\alpha j}(\mathbf{r}_{21})$ and in the integration limits of eq 16. In the next two subsections, we apply this equation to the cases of cylindrical and spherical nanopores.

1. The Cylindrical Nanopore. The interaction potential between an ion of species j and a cylindrical nanopore described in Figure 1b depends only on the *cylindrical* radial distance, r,

and is given by

$$u_{\alpha j}(r) = \begin{cases} -\frac{4\pi q_j}{\epsilon}[R\sigma_i \ln(R) + (R+d)\sigma_o \ln(R+d)] \\ \qquad r < R - a/2 \\ \infty \qquad R - a/2 \leq r \leq R + d + a/2 \\ -\frac{2\pi q_j}{\epsilon}[R\sigma_i + (R+d)\sigma_o]\ln(r) \\ \qquad r > R + d + a/2 \end{cases} \qquad (17)$$

In the same way, the distribution function depends only on the cylindrical radial coordinate; i.e., $g_{\alpha j}(\mathbf{r}_{21}) \equiv g_{\alpha j}(r)$. Also, $h_{\alpha m}(\mathbf{r}_{23}) \equiv h_{\alpha m}(r_3)$. By using eq 17 in eq 16, one can easily infer that $g_{\alpha j}(r) = 0$, or equivalently, $h_{\alpha j}(r) = -1$ for $R - a/2 \leq r \leq R + d + a/2$. The use of cylindrical coordinates, where $r_{13} = r^2 + r_3^2 + z_3^2 - 2rr_3\cos\phi_3$ and $d\mathbf{r}_3 = r_3\,dr_3\,dz_3\,d\phi_3$, with $0 < \phi_3 \leq 2\pi$, $-\infty < z_3 < \infty$, and $0 \leq r_3 < \infty$, results in

$$g_{\alpha j}(r) = \exp\left\{\frac{4\pi\beta q_j}{\epsilon}[R\sigma_i \ln R + (R+d)\sigma_o \ln(R+d)] + \right.$$
$$\frac{2\pi\beta q_j}{\epsilon}\int_0^\infty \rho_d(r_3)f_c(r,r_3)\,dr_3 + q_j\int_0^\infty \rho_d(r_3)L(r,r_3)\,dr_3 + $$
$$\left. \int_0^\infty \rho_s(r_3)K(r,r_3)\,dr_3\right\} \qquad (18)$$

for $r < R - a/2$ and

$$g_{\alpha j}(r) = \exp\left\{\frac{4\pi\beta q_j}{\epsilon}[R\sigma_i + (R+d)\sigma_o]\ln(r) + \right.$$
$$\frac{2\pi\beta q_j}{\epsilon}\int_0^\infty \rho_d(r_3)f_c(r,r_3)\,dr_3 + q_j\int_0^\infty \rho_d(r_3)L(r,r_3)\,dr_3 + $$
$$\left. \int_0^\infty \rho_s(r_3)K(r,r_3)\,dr_3\right\} \qquad (19)$$

for $r > R + d + a/2$. With the definitions $\rho_d(r_3) \equiv \sum_{m=1}^{2}\rho_m q_m h_{\alpha m}(r_3)$, $\rho_s(r_3) \equiv \sum_{m=1}^{2}\rho_m h_{\alpha m}(r_3)$, and

$$f_c(r,r_3) = r_3 \ln\left(\frac{r^2 + r_3^2 + |r^2 - r_3^2|}{2}\right)$$

$$K(r,r_3) = \int_{-\infty}^{\infty}\int_0^{2\pi}c^{hs}(r_{13})r_3\,d\phi_3\,dz_3$$

$$L(r,r_3) = \int_{-\infty}^{\infty}\int_0^{2\pi}c^{sr}(r_{13})r_3\,d\phi_3\,dz_3 \qquad (20)$$

which result from the first, second, and third integral terms in eqs 18 and 19, respectively. In cylindrical geometry, these integrals are[32]

$$K(r,r_3) = \begin{cases} 0 \qquad r_3 < r - a \\ -4r_3\int_0^{\phi_0}\left(c_1 J_0 + 6\eta c_2 J_1 + \frac{1}{2}\eta c_3 J_3\right)d\phi \\ \qquad r - a \leq r_3 \leq r + a \\ 0 \qquad r_3 > r + a \end{cases} \qquad (21)$$

and

$$L(r,r_3) = \begin{cases} 0 \qquad r_3 < r - a \\ -\frac{4r_3\beta}{\epsilon}\int_0^{\phi_0}\left(J_2 - \frac{2\Gamma J_0}{1+\Gamma a} + \frac{\Gamma^2 J_1}{(1+\Gamma a)^2}\right)d\phi \\ \qquad r - a \leq r_3 \leq r + a \\ 0 \qquad r_3 > r + a \end{cases} \qquad (22)$$

where

$$J_0 \equiv \int_0^{z_0} dz \tag{23}$$

$$J_1 \equiv \int_0^{z_0} r_{13} \, dz \tag{24}$$

$$J_2 \equiv \int_0^{z_0} \frac{1}{r_{13}} \, dz \tag{25}$$

$$J_3 \equiv \int_0^{z_0} r_{13}^3 \, dz \tag{26}$$

2. The spherical nanopore. In the spherical charged pore case, we have

$$u_{\alpha j}(r) = \begin{cases} -\dfrac{4\pi q_j}{\epsilon}[R\sigma_i + (R+d)\sigma_o] \\ \qquad r < R - a/2 \\ \infty \qquad R - a/2 \le r \le R + d + a/2 \\ -\dfrac{4\pi q_j}{r\epsilon}[R^2\sigma_i + (R+d)^2\sigma_o] \\ \qquad r > R + d + a/2 \end{cases} \tag{27}$$

In this case, r is the radial spherical coordinate, $r_{13} = r^2 + r_3^2 + 2rr_3 \cos\theta_3$, $d\mathbf{r}_3 = r_3^2 \sin\theta_3 \, dr_3 \, d\theta_3 \, d\phi_3$, with $0 < \phi_3 \le 2\pi$, $-\pi < \theta_3 < \pi$, and $0 \le r_3 < \infty$. We obtain

$$g_{\alpha j}(r) = \exp\left\{ \frac{4\pi\beta q_j}{\epsilon}[R\sigma_i + (R+d)\sigma_o] + \right.$$
$$\frac{2\pi\beta q_j}{\epsilon} \int_0^\infty \rho_d(r_3) f_s(r,r_3) \, dr_3 + q_j \int_0^\infty \rho_d(r_3) L(r,r_3) \, dr_3 +$$
$$\left. \int_0^\infty \rho_s(r_3) K(r,r_3) \, dr_3 \right\} \tag{28}$$

for $r < R - a/2$, and

$$g_{\alpha j}(r) = \exp\left\{ \frac{4\pi\beta q_j}{r\epsilon}[R^2\sigma_i + (R+d)^2\sigma_o] + \right.$$
$$\frac{2\pi\beta q_j}{\epsilon} \int_0^\infty \rho_d(r_3) f_s(r,r_3) \, dr_3 +$$
$$\left. q_j \int_0^\infty \rho_d(r_3) L(r,r_3) \, dr_3 + \int_0^\infty \rho_s(r_3) K(r,r_3) \, dr_3 \right\} \tag{29}$$

for $r > R + d + a/2$, where

$$f_s(r,r_3) = -\left(\frac{r_3}{r}\right)(r + r_3 - |r - r_3|)$$

$$K(r,r_3) = 2\pi \int_{-\pi}^\pi c^{hs}(r_{13}) r_3^2 \sin\theta_3 \, d\theta_3$$

$$L(r,r_3) = 2\pi \int_{-\pi}^\pi c^{sr}(r_{13}) r_3^2 \sin\theta_3 \, d\theta_3 \tag{30}$$

$\rho_d(r_3)$ and $\rho_s(r_3)$ have the same definition as the cylindrical case, and the integrals in eq 30 are[51]

$$K(r,r_3) = -2\pi r_3^2\left(c_1 J_0 + 6\eta c_2 J_1 + \frac{1}{2}\eta c_3 J_3\right) \tag{31}$$

and

$$L(r,r_3) = \frac{-2\pi\beta r_3^2}{\epsilon}\left(J_{-1} - \frac{2\Gamma J_0}{1 + \Gamma a} + \frac{\Gamma^2 J_1}{(1 + \Gamma a)^2}\right) \tag{32}$$

and in this case

$$J_i \equiv \frac{1}{(i+2)rr_3}(a^{i+2} - |r - r_3|^{i+2}) \tag{33}$$

The solution of eqs 18 and 19 gives the reduced concentration profiles inside and outside the cylindrical pore, $g_{\alpha j}(r)$ (eqs 28 and 29 correspond to the spherical cavity). These equations show that the inside fluid structure depends on the outside fluid distribution. Therefore, it is said that the confined and unconfined fluids are correlated.[27,33] In the past, it has been shown that this correlation may manifest itself as a VLEC.[26,34]

3. Electroneutrality Condition and Pressure Equations. In the cylindrical case, we have that the induced charge densities, σ'_{in} and σ'_{out}, inside and outside the pore, respectively, are given by

$$\sigma'_{in} = -\frac{1}{R} \int_0^{R-a/2} r\rho_{el}(r) \, dr$$

$$\sigma'_{out} = -\frac{1}{R+d} \int_{R+d+a/2}^\infty r\rho_{el}(r) \, dr \tag{34}$$

whereas for the spherical nanopore we have

$$\sigma'_{in} = -\frac{1}{R^2} \int_0^{R-a/2} r^2\rho_{el}(r) \, dr$$

$$\sigma'_{out} = -\frac{1}{(R+d)^2} \int_{R+d+a/2}^\infty r^2\rho_{el}(r) \, dr \tag{35}$$

In both cases (cylindrical and spherical), we have defined $\rho_{el}(r) = \sum_{i=1}^2 ez_i\rho_i g_{\alpha i}(r)$.

As we mentioned before, the general electroneutrality condition (GEC) is always satisfied and implies

$$R\sigma'_{in} + (R+d)\sigma'_{out} = R\sigma_i + (R+d)\sigma_o$$

$$R^2\sigma'_{in} + (R+d)^2\sigma'_{out} = R^2\sigma_i + (R+d)^2\sigma_o \tag{36}$$

in cylindrical and spherical geometry, respectively. However, VLEC implies $\sigma'_{in} \ne -\sigma_i$ and $\sigma'_{out} \ne -\sigma_o$. This effect (VLEC) has been observed for unsymmetrical charge densities ($\sigma_i \ne \sigma_o$) and for high fluid confinement.[26,27,34]

Another interesting phenomena occurs in the analysis of the pressure difference

$$p(R) = p_0(R) - p_{bulk}(R) \tag{37}$$

between the confined (p_0) and unconfined (p_{bulk}) fluids, which also can be expressed as

$$p(R) = p_C(R) + p_E(R) \tag{38}$$

where $p_C(R)$ and $p_E(R)$ are the contact and electrical components, respectively. For the spherical nanopore, $p_C(R)$ and $p_E(R)$ are given by[12]

$$p_C(R) = k_B T[\rho_{\alpha s}(R - a/2) - \rho_{\alpha s}(R + d + a/2)] \tag{39}$$

$$p_E(R) = -\frac{2\pi}{\epsilon}[\gamma_{in}^2(\sigma'_{in})^2 - \gamma_{out}^2(\sigma'_{out})^2] -$$
$$\frac{\epsilon}{4\pi}\left[\frac{1}{(R - a/2)^2} \int_0^{R-a/2} rE^2(r) \, dr + \right.$$
$$\left. \frac{1}{(R + d + a/2)^2} \int_{R+d+a/2}^\infty rE^2(r) \, dr\right] \tag{40}$$

Van der Waals-like Isotherms in Confined Electrolyte

J. Phys. Chem. B, Vol. 111, No. 8, 2007 **2037**

with

$$\gamma_{in} = \frac{R}{R - a/2} > 1 \qquad (41)$$

and

$$\gamma_{out} = \frac{R + d}{R + d + a/2} < 1 \qquad (42)$$

Note that, as R decreases, the inward contribution of the confined fluid, $-(2\pi/\epsilon)\gamma_{in}^2(\sigma'_{in})^2$, tends to more negative values at a high rate, whereas the outside contribution, $(2\pi/\epsilon)\gamma_{out}^2(\sigma'_{out})^2$, remains positive and decreases at a low rate. This preliminary conclusion is a consequence of that fact that $\gamma_{in} \rightarrow \infty$ as $R \rightarrow a/2$; meanwhile, $\gamma_{out} \rightarrow 0$ as $(R + d) \rightarrow 0$. Evidently, it depends on the behavior of σ'_{in} and σ'_{out} as a function of R.

In the cylindrical charged nanopore the pressure components are given by

$$p_C(R) = k_BT[\rho_{\alpha s}(R - a/2) - \rho_{\alpha s}(R + d + a/2)] \quad (43)$$

$$p_E(R) = -\frac{2\pi}{\epsilon}[\gamma_{in}(\sigma'_{in})^2 - \gamma_{out}(\sigma'_{out})^2] - \frac{\epsilon}{8\pi}\left[\frac{1}{(R - a/2)}\int_0^{R-a/2} E^2(r)\,dr + \frac{1}{(R + d + a/2)}\int_{R+d+a/2}^{\infty} E^2(r)\,dr\right] \quad (44)$$

where $\rho_{\alpha s}(r) = \sum_{i=1}^{2}\rho_i g_{\alpha i}(r)$, $E(r)$ is the local electrical field, and γ_{in} and γ_{out} are given by eqs 41 and 42, respectively.

4. The Planar Slit Nanopore. In order to have a full description of the geometry-confinement effect, besides the cylindrical and spherical geometries, we compare with a planar slit pore. The model consists of two infinite charged parallel plates of thickness d, separated by a distance $\tau = 2R$. As in cylindrical and spherical geometries, R is the distance from the inner pore's surface to the center. The planar nanopore has uniformly distributed surface charge densities, σ_i and σ_o on the inner and outer plates' surfaces. A detailed derivation of the HNC/MSA and pressure equations for this geometry is given in refs 52 and 53. The pressure components are given as

$$p_C(R) = k_BT[\rho_{\alpha s}(R - a/2) - \rho_{\alpha s}(R + d + a/2)] \quad (45)$$

$$p_E(R) = -\frac{2\pi}{\epsilon}[(\sigma'_{in})^2 - (\sigma'_{out})^2] \qquad (46)$$

and the induced charge densities, σ'_{in} and σ'_{out}, inside and outside the pore, respectively, are given by

$$\sigma'_{in} = \int_0^{R-a/2}\rho_{el}(y)\,dy$$

$$\sigma'_{out} = \int_{R+d+a/2}^{\infty}\rho_{el}(y)\,dy \qquad (47)$$

having $\rho_{\alpha s}(x)$ and $\rho_{el}(x)$ the same meaning as for spherical and cylindrical geometries. Note that eq 40 for p_E in spherical geometry depends quadratically on γ_{in}, γ_{out}, $1/(R - a/2)$, and $1/(R + d + a/2)$, whereas for cylindrical geometry (eq 44) it depends linearly on the same factors. Planar geometry, eq 46, is recovered from both, eqs 40 and 44, in the limit of R $\rightarrow \infty$, which implies that $\gamma_{in} = \gamma_{out} = 1$ and $1/(R - a/2) = 1/(R + d + a/2) = 0$. On the basis of this, one can say that the confinement effect is higher in spherical geometry than in cylindrical, which in turn, is higher than in planar geometry.

Let us now define the deviation of local electroneutrality condition (LEC), $\Delta\sigma$, as

$$\Delta\sigma_{in} = \sigma'_{in} - \sigma_i \qquad (48)$$

$$\Delta\sigma_{out} = \sigma'_{out} - \sigma_o \qquad (49)$$

$\Delta\sigma_{in} = 0$ and $\Delta\sigma_{out} = 0$ imply that the LEC is satisfied. If $\Delta\sigma_{in} < 0$, this implies undercompensation by the electrolyte of the inner pore surface charge, whereas $\Delta\sigma_{in} > 0$ implies overcompensation.

III. Results and Discussion

The thermodynamical and structural properties of the bulk RPM electrolyte can be described in terms of the following parameters[36,54]

$$\xi_{ij} \equiv \frac{q_iq_j\beta}{a\epsilon} \qquad i, j = +, - \qquad (50)$$

$$\eta_i \equiv \frac{\pi}{6}\rho_i a^3 \qquad i, j = +, - \qquad (51)$$

where ξ_{ij} quantifies the strength of the ion−ion electrostatic interaction between two ions of species i and j; this is referred to as the ion−ion Coulomb coupling. Notice that ξ is inversely proportional to temperature. The second parameter, η_i, quantifies the particle's volume fraction for the species i. Because we consider symmetrical electrolytes, $\eta_+ = \eta_- \equiv \eta/2$ and $\xi_{++} = \xi_{--} = |\xi_{+-}| \equiv \xi$. We therefore omit the subindexes. In our discussion, the effects produced by varying z_i, ρ_i, and ϵ will be associated with variations of η and ξ. Hereinafter, unless otherwise indicated, $d = a$, $\sigma \equiv \sigma_i = \sigma_o = 0.272$C/m^2, and $\epsilon = 78.5$. The bulk electrolyte concentration is $\rho_s = 0.971$ M and the ionic diameter (a) = 4.25Å, so that $\eta = 0.047$. In Figure 2, the pressure, $p(R)$, is plotted as a function of the pore size, for a divalent electrolyte ($z = 2$) confined by a spherical cavity and cylindrical and planar slit nanopores, in units of ρk_BT. Notice that, for a monovalent electrolyte ($z = 1$), if $\epsilon = 78.5/4$ the results will be identical to the divalent case discussed here.

Three different values of the Coulomb coupling parameter, ξ, were chosen for each geometry: for the spherical cavity, $\xi = 6.16$, 6.49, and 6.90 ($T = 325$, 308.5, and 290 K, respectively), whereas for the cylindrical and planar slit pore $\xi = 5.72$, 5.98, and 6.90 ($T = 350$, 334.6, and 290 K). For the three geometries, when R is of the order of hundreds of ionic diameters, the net pressure on the confining wall, $p(R)$, is negligible, meaning that the pressures of the confined (p_0) and unconfined (p_{bulk}) fluids are balanced (see eq 37). For the spherical and cylindrical nanopores, there is a general tendency of $p(R)$ to become negative and to decrease as R decreases. For $\xi = 6.90$, there is an interval of R where $p(R)$ increases with R; however for these two geometries, in the 2:2 electrolyte case, the pressure is always negative. For 1:1 electrolytes, typical ξ values are around 1.6, and the pressure is, in general, positive.

These curves are analogous to isotherms for a bulk fluid in a *PVT* liquid−vapor phase diagram. Furthermore, curve loops for $\xi = 6.90$ in the spherical and cylindrical geometries resemble the prediction of the van der Waals equation of state for a bulk fluid. The loops predicted by the van der Waals equation of state define the coexistence region by the equal area Maxwell's rule, whereas the location of maxima and minima define the spinodal curve. In VW theory, the pressure prediction inside the spinodal curve is unphysical, because it implies a negative compressibility; however, in our case it is real. This is due to
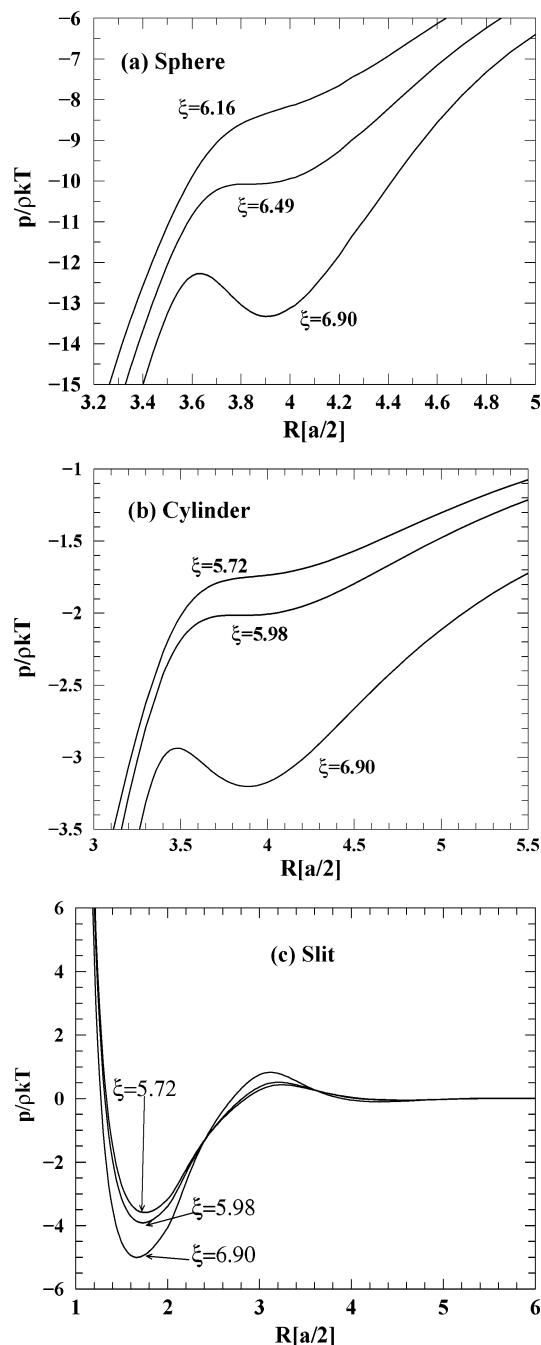
Figure 2. Pressure as a function of the nanopore size, *R*, for (a) spherical, (b) cylindrical, and (c) slit-like nanopores. In all cases, $\sigma = 0.272 \text{C/m}^2$ and $\eta = 0.047$.

the confinement by the charged walls that stabilize the system. However, it should be pointed out that, although the VW theory is for a bulk fluid, in our case, this negative compressibility is within the pore cavity, and the total system pressure, i.e., the pore immersed in the fluid, is constant.

In the confined fluids, by progressively increasing the temperature (decreasing ξ), the loops become less pronounced, and eventually, they disappear. We call the "critical'' isotherm, in analogy with the van der Waals theory, that where the maximum and minimum disappear and there is only an inflection point. In fact, we can talk of a "spinodal" curve. The critical isotherm occurs at $\xi_c = 6.49$ ($T_c = 308.5$ K) in the spherical shell and at $\xi_c = 5.98$ ($T_c = 334.6$ K) in the cylindrical pore. By increasing T beyond the critical temperature, a new class of curves occurs with no maxima and minima in which

$p(R)$ is only monotonically decreasing. It should be noticed that, in general, by decreasing ξ (increasing *T*), $|p(R)|$ decreases, which is a consequence of the decrement in the Maxwell stress tensor (MST) contribution to the total pressure, $p_E(R)$. On the other hand, the absolute values of $p(R)$ are higher in the spherical shell than in the cylindrical pore, because in the spherical shell the fluid confinement is higher than in the cylindrical pore. Although in the liquid vapor coexistence region there is a phase transition, in our case, we find that there is a charge separation; i.e., there is a region of only coions surrounded by only counterions, which in turn are next to the cavity wall.

For the slit-like nanopore (Figure 2c), the pressure has a completely different behavior from that in the spherical and cylindrical geometries. In planar geometry, $p(R)$ oscillates around zero and becomes increasingly positive for small values of *R*, whereas, in the spherical and cylindrical nanopores, the pressure is always negative. Although not shown, for $R < 3(a/2)$, in the cylindrical and spherical geometries, $p(R)$ is monotonically decreasing. Compared to the spherical and cylindrical pores, the absolute value of the slit nanopore pressure is much smaller and of much shorter range, and the whole slit pressure curve is shifted to the left. In fact, our results show that the more "open" the pore is, the shorter the range of $p(R)$.

The negative pressure (Figure 2, parts a and b) can be better understood in Figure 3 where $p(R)$ is analyzed in terms of its contact ($p_C(R)$) and electrical ($p_E(R)$) components, given by eqs 39−46. Notice that $p_E(R)$ is negative in the spherical and cylindrical cases, whereas it oscillates between positive and negative for the slit pore. In spherical and cylindrical geometries, the inward pressure is ruled by p_E, and although the oscillatory behavior is also due to p_C, the total pressure is dominated by the electrical component. On the other hand, for the slit-like pore, see eqs 45 and 46; the behavior of p_T is dictated by p_C, implying that the contact pressure component dominates over the Maxwell stress tensor (MST) component, $p_E(R)$. Although not shown, for the 1:1 electrolyte, i.e., low values of ξ, the pressure for spherical and cylindrical pores is positive, except at very small pore radii. This implies that the inward or repulsive nature of the pressure is a result of a competition between the MST and contact contributions.

Figure 4 shows a further analysis of $p(R)$ by means of its subcomponents. For the spherical case, the internal pressure is decomposed as (see Figure 4a) $p_0 = p_1^{in} + p_2^{in} + p_3^{in}$, where

$$p_1^{in} = k_B T \rho_{\alpha s}(R - a/2) \tag{52}$$

$$p_2^{in} = -\frac{2\pi}{\epsilon}(\sigma'_{in}\gamma_{in})^2 \tag{53}$$

$$p_3^{in} = -\frac{\epsilon}{4\pi(R - a/2)^2} \int_0^{R-a/2} rE^2(r)\,dr \tag{54}$$

The external pressure is analogously decomposed in subcomponents as $p_{bulk} = p_1^{out} + p_2^{out} + p_3^{out}$, with

$$p_1^{out} = k_B T \rho_{\alpha s}(R - a/2) \tag{55}$$

$$p_2^{out} = -\frac{2\pi}{\epsilon}(\sigma'_{out}\gamma_{out})^2 \tag{56}$$

$$p_3^{out} = -\frac{\epsilon}{4\pi(R + d + a/2)^2} \int_{R+d+a/2}^{\infty} rE^2(r)\,dr \tag{57}$$

Notice that the subcomponents of p_{bulk}, p_1^{out}, and p_2^{out} (Figure 4b) nearly cancel each other $\forall\ R$ and give $p_{bulk} = p_1^{out} + p_2^{out} +$

Van der Waals-like Isotherms in Confined Electrolyte

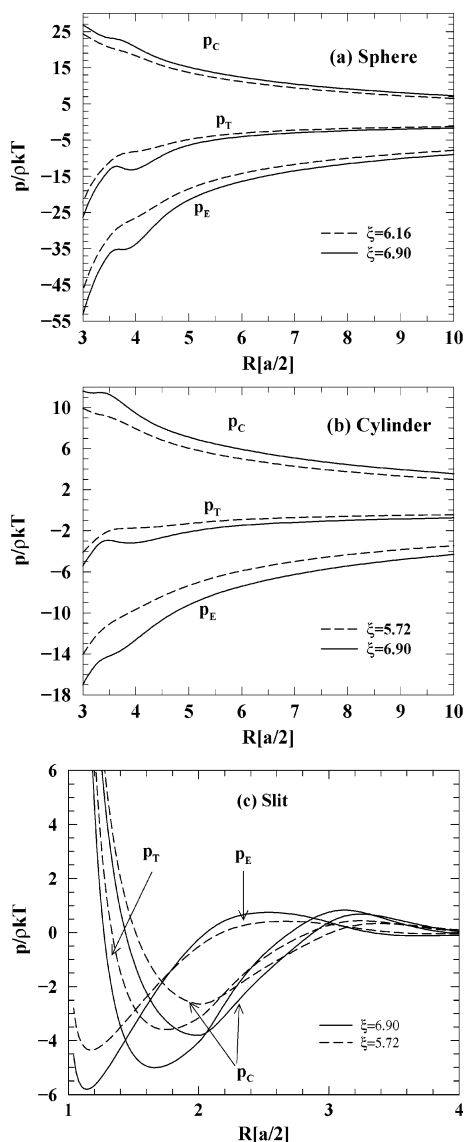*J. Phys. Chem. B, Vol. 111, No. 8, 2007* **2039**

Figure 3. Contact and electrical components of pressure, as a function of the nanopore size, R, for (a) spherical, (b) cylindrical, and (c) slit-like nanopores. In all the curves, $\sigma = 0.272 \text{C/m}^2$ and $\eta = 0.047$.
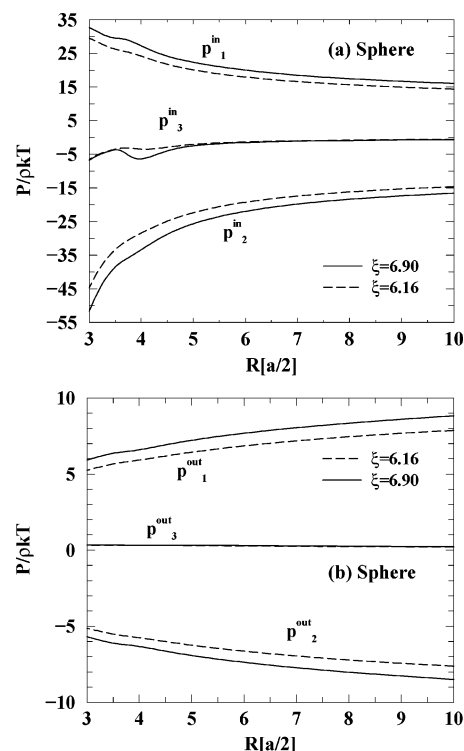

Figure 4. Subcomponents of pressure as a function of the nanopore radius, R, for the spherical case: (a) corresponds to the internal and (b) the external pressure subcomponents. In all cases, $\sigma = 0.272 \text{C/m}^2$ and $\eta = 0.047$.
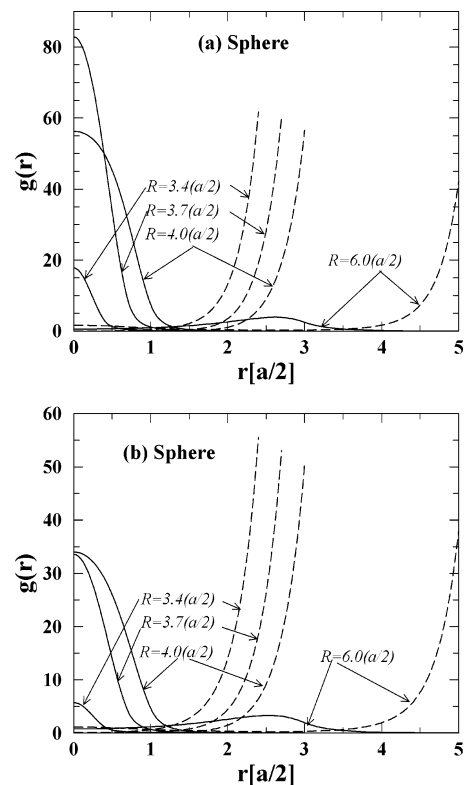

Figure 5. Reduced concentration profiles (RCP) for a 2:2, 0.971 M ($\eta = 0.047$) electrolyte, confined by a spherical pore with $\sigma = 0.272$ C/m^2: (a) $\xi = 6.9$ ($T = 290$ K) and (b) $\xi = 6.16$ ($T = 325$ K). Each plot contains the RCPs for $R = 6.0(a/2)$, $4.0(a/2)$, $3.7(a/2)$, $3.4(a/2)$. Solid lines are for coions, and the dashed ones are for counterions.

$p_3^{\text{out}} \approx \text{cst} > 0$ for both cases ($\xi = 6.9$ and 6.16). Hence, the oscillatory behavior of $p(R)$ is mostly attributed to p_3^{in} as can be seen in Figure 4a. From eq 53, it is clear that this oscillatory behavior of $p_3^{\text{in}}(R)$ is attributed to the different ionic configurations adopted by the fluid as a function of R, which in turn produce different electric field profiles, $E(r)$, inside the pore. We will discuss this point later in relation to Figure 5.

Note that $p_0 = p_1^{\text{in}} + p_2^{\text{in}} + p_3^{\text{in}} < 0$ and $|p_{\text{bulk}}| < |p_0|$; therefore, $p(R) = p_0 - p_{\text{bulk}} < 0$ implies a real inward pressure on the pore produced by the confined fluid. In fact, $p_0 < 0$ is attributed to the electrical field of the confined fluid because counterions outnumber coions inside the pore, and in consequence, the confined fluid has a net negative charge that exerts an inward force on the pore's positive wall. This is in fact the usual effect of the MST pressure component, only that it is enhanced by the confinement. Such a negative force dominates over the outward contact force, p_C. As R decreases, the inward force, p_2^{in}, has more negative values at a high rate, whereas its counterbalancing force, p_2^{out}, remains positive and decreases (see discussion below eq 42). Although it is not shown for $R < 3(a/2)$, $p(R)$ decreases up to the order of -10^3 for the spherical pore and to -10^2 for the cylindrical pore. The behavior of $p(R)$

is completely different for the slit-like nanopore, which for small values of R becomes positive. This is related to the much lower

values of p_2^{in}, which in turn is due to the lower intensity of the electrical field (see eq 46 and discussion below).

We now analyze the isotherm loops in terms of the charge distribution inside of the pores. Outside the spherical and cylindrical pores, the reduced concentration profiles (RCP) have the typical behavior for an electrolyte next to a charged wall and have no qualitative changes as a function of the pore size (not shown). The contact counterion concentration, however, decreases as the radius decreases in both geometries.

Inside the pores, if R is sufficiently large, the ions are mixed and resemble very much the qualitative behavior seen at the outside of the pore. However, as the pore radius decreases, the ions progressively separate in two phases; that is, counterions form a layer contiguous to the pore's wall, whereas coions are segregated toward the pore's center. This is manifested as the appearance of a maximum of $g_+(r)$ at $r = 0$, whereas it is practically zero at $r = R - a/2$. Counterions behave in the opposite way; i.e., the maximum of $g_-(r)$ is at $r = R - a/2$, whereas it vanishes at $r = 0$. This segregation effect starts at $R \approx 5(a/2)$.

Figure 5 show RCP for a 2:2, 0.971 M electrolyte confined by a spherical shell. Figure 5a shows the RCPs for $\xi = 6.9$ ($T = 290$ K), whereas Figure 5b shows RCPs for $\xi = 6.16$ ($T = 325$ K), i.e., corresponding to the top and bottom curves in Figure 2a, respectively. In the isotherm for $\xi = 6.90$ (Figure 5a), for $R = 6.0(a/2)$, counterions are adsorbed to the wall, whereas coions are away from it; thus, $g_-(R - a/2) \gg 1$ and $g_+(r - a/2) \rightarrow 0$. However, for $2(a/2) \lesssim r \lesssim 3(a/2)$, we have more coions than counterions, and at $r \approx 0$, both, $g_+(r) \approx g_-(r) \approx 1$, implying that coions and counterions are well mixed at the pore's center and, in general, throughout the pore. This concentration profile is very much like any other at a charged interface, in the sense that counterions are next to the wall, coions are repelled from it, and coions and counterions are mixed at different degrees, as a function of their distance to the wall. Curves for $R = 4.0(a/2)$, $3.7(a/2)$, and $3.4(a/2)$ are a successive sequence in R where coions and counterions are completely separated. The contact value of the counterions profile, $g_-(R - a/2)$, slightly increases as R decreases. However, major variations are observed in the maximum of coions concentration profiles at the center of the pore, $g_+(0)$. A reduction of the pore radius from $4(a/2)$ to $3.7(a/2)$ produces an important increment of $g_+(0)$, whereas by decreasing R from $3.7(a/2)$ to $3.4(a/2)$ produces the opposite effect. Hence, $g_+(0)$ has a non-monotonic behavior that starts to increase at $R \approx 5.0(a/2)$ with a maximum, defined as g_+^{max}, at $R \approx 3.7(a/2)$, from where it decreases to zero for $R \lesssim 3.0(a/2)$, i.e., when coions are completely expelled from the pore.

The RCPs for $\xi = 6.16$ (Figure 5b) also show a coion segregation toward the pore's center and separated from counterions, which form a shell next to the pore's wall. However, there are important differences with respect to the profiles for $\xi = 6.90$. Here, g_+^{max} is not as pronounced as for $\xi = 6.90$; i.e., although the increase of $g_+(0)$ starts at $R \approx 5(a/2)$, g^{max} is at $R \approx 4(a/2)$, from where it starts to decrease: for $\xi = 6.16$, g_+^{max} is less than half that for $\xi = 6.9$ and occurs at a larger pore size, implying that at higher temperature the coions are expelled from the pore more easily. There are two features we wish to point out, in addition to the charge separation for small pores: (i) the higher absorption for the $\xi = 6.9$ ($T = 290$ K) case, which is seen in higher values of $g_i(r)$, as compared to the $\xi = 6.16$ ($T = 325$ K) case (see Figures 5a and 5b). Clearly, a lower temperature implies a higher adsorption. (ii) The other relevant feature is the higher localization of coions at the pore's

center, for $\xi = 6.9$, between $R = 4(a/2)$ and $3.5(a/2)$, implying a higher polarization of the confined charged fluid. This higher polarization, in turn, explains the decrease of the inward pressure, due to a decrease of the MST contribution, and an increment of the contact pressure contribution: see p_1^{in} and p_3^{in}, in Figure 4a, for $3.5(a/2) \leq R \leq 4(a/2)$ and Figure 3a.

For the $\xi = 6.16$ case, the coion localization does not seem to be enough to counterbalance the temperature entropic contribution, and hence, no decrease of the inward pressure is observed (see Figures 4a and 5b).

In the cylindrical pore, the behavior of $p(R)$ and RCPs for different pore radii is qualitatively similar to that described in the spherical case. This means that, for some values of R, there is a charge separation inside the pore and a segregation of coions toward the cylinder axis, and when the ξ parameter is above a "critical" value, the isotherms present van der Waals-like loops. In the cylindrical geometry, in general, $g_+(0)$ and $g_-(R - a/2)$ are smaller than for the spherical pore, which we attribute to less confinement in the cylinder than in the spherical pore, and hence less localization of the pore's fluid, which implies a minor decrement of the inward pressure, for $\xi = 6.9$ and for $3.5(a/2) \lesssim R \lesssim 4.0(a/2)$. The shift of the pressure hump to the left (narrower pore radius) with respect to the spherical pore in the cylindrical case can be explained in terms of the need of an equivalent confinement. The RCPs for cylindrical pores are not shown.

To further quantify the ionic absorption in the pore, we compute the particles volume fraction inside the pore as

$$\bar{\eta}_i^x = \frac{\pi a^3 \bar{\rho}_i}{6} \tag{58}$$

where $\bar{\rho}_i$ is the mean concentration inside the pore for species i with $i = +, -$, $x = $ s for the sphere and $x = $ c for the cylinder, and the total particle volume fraction is $\bar{\eta}_T^x = \bar{\eta}_+^x + \bar{\eta}_-^x$. For the spherical nanopore, we have

$$\bar{\eta}_i^s = \frac{\pi}{2}\left(\frac{a}{R}\right)^3 \int_0^{R-a/2} \rho(y)y^2 \, dy \tag{59}$$

whereas for the cylindrical nanopore we have

$$\bar{\eta}_i^c = \frac{\pi a^3}{3R^2} \int_0^{R-a/2} \rho(y)y \, dy \tag{60}$$

In Figure 6, we show $\bar{\eta}_i^x$ for coions (+), counterions (−), and total (T), as a function of the pore radius. The results for the spherical shell (Figure 6a) correspond to the same conditions as in Figure 2a, i.e., $\xi = 6.16$, 6.49, and 6.90, whereas for the cylindrical pore (Figure 6b) they correspond with Figure 2b, i.e., $\xi = 5.72$, 5.98, and 6.67. The general features of the particle volume fraction curves are as follows: (a) More confinement implies a higher volume fraction, $\bar{\eta}_T^s$, and a lower number of particles; i.e., although the total number of particles decreases, as R decreases, the volume size decreases at a higher rate, see eqs 59 and 60. (b) Higher temperatures, i.e., lower values of ξ, imply less particle absorption. (c) More open geometries (cylindrical case) imply less absorption.

For larger values of R, $\bar{\eta}_T^x$, $\bar{\eta}_-^x$, and $\bar{\eta}_+^x$ tend asymptotically to a limiting value depending on the pore's charge and electrolyte temperature and concentration. Hence, for $R > 5(a/2)$ the $\bar{\eta}_i^x$ curves, for the three values of ξ, are nearly parallel as R increases. Thus, an interesting behavior is the hump observed for $3.5(a/2) < R < 4.5(a/2)$, for the $\xi = 6.9$, $\bar{\eta}_T^s$ curve
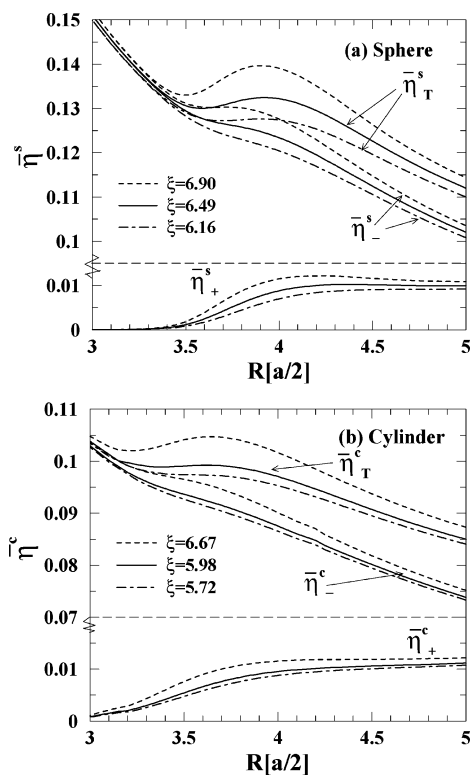
Van der Waals-like Isotherms in Confined Electrolyte

J. Phys. Chem. B, Vol. 111, No. 8, 2007 **2041**

Figure 6. Particle volume fraction inside the pores, $\bar{\eta}_i^x$, for counterions ($-$), coions ($+$), and total (T), as a function of R, for (a) spherical and (b) cylindrical nanopores. In all cases, $\eta = 0.047$ ($\rho_s = 0.971$ M) and $\sigma = 0.272$ C/m^2.

Figure 7. Deviation from electroneutrality, as a function of R, at the inside ($\Delta\sigma_{in}$) and outside ($\Delta\sigma_{out}$) of the spherical cavity. In both cases, $\eta = 0.047$ ($\rho_s = 0.971$ M) and $\sigma = 0.272$ C/m^2.

Figure 8. Representation of the forces in a cylindrical geometry. The process is similar in spherical geometry.

(see Figure 6a). For $\xi = 6.16$, there is also a $\bar{\eta}_T^s$ hump in the same region. This hump, however, is less pronounced than for the $\xi = 6.9$ case due to the higher temperature.

Let us focus, for a moment, on this $\xi = 6.9$ case: in the region of interest, $\bar{\eta}_-^s$ reaches a plateau and $\bar{\eta}_+^s$ decreases at a larger rate than, for example, the $\xi = 6.16$ case; hence, $\bar{\eta}_T^s$ is seen to decrease for $3.5(a/2) < R < 4(a/2)$. We recall that, for this interval, in R, the coions concentrate around the center of the pore (see Figure 5a), with high values of $g_+(0)$, suggesting an increase of coion concentration. However, in Figure 6a, we see the opposite; i.e., coions are being expelled out of the pore at a high rate. Therefore, these two results suggest that indeed although the coions are being expelled out of the pore, they are much more localized and hence decreasing the electrical field and the MST inward pressure. Further, if we look at the counterion contact value, $g_-(R - a/2)$, in Figure 5a, we see a modest but still an increment, as R decreases, which explains an increment in the contact pressure component, p_1^{in}.

In a closed system, an increment of temperature implies, in general, a higher pressure. In our case, we see the opposite effect, due to the decrease of the total number of particles. In addition, in confinement by charged pores, the pressure behavior is dictated by the MST. The outstanding demixing of coions and counterions translates into an optimal use of the available space, which we see as a decrease of $\bar{\eta}_T^s$, for $3.5(a/2) < R < 4(a/2)$, i.e., a decrease of the particle excluded volume and hence an increase of the available volume and thus an increase in the system entropy. This charge ordering decreases the MST inward pressure. Although a demixing, in general, implies a decrease of entropy, from $R = 4.0(a/2)$ to $R = 3.5(a/2)$, what we see is an increase of accessible volume, hence an increment of entropy. The demixing really starts at $R \approx 6(a/2)$, and we see an increase
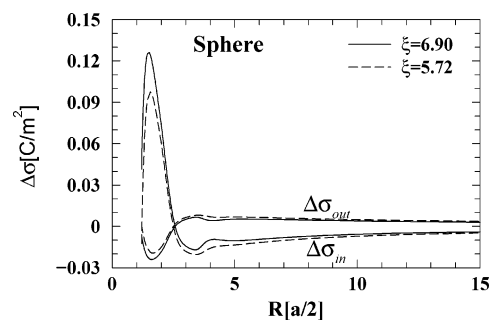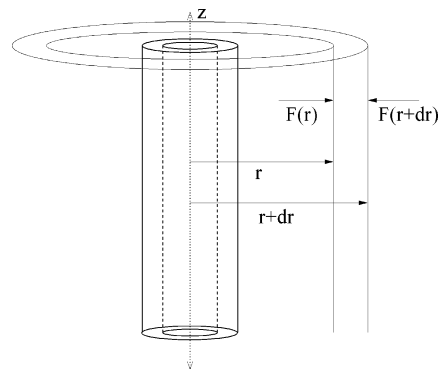
of the excluded volume, hence a decrease of accessible volume and thus an increase of entropy (see Figure 6a). Notice that the entropy behavior is subjected to three effects: (1) the ordering of particles trying to optimize the accessible volume; (2) the decrease of the total volume and hence the decrease of the accessible volume due to the decrease of the pore size, and (3) the ion release implies an increase of the accessible volume. The total pore size decreases as R^3, whereas the other two are more difficult to characterize, but the total effect is depicted in Figure 6a. Clearly, below $R \approx 3.5(a/2)$, the rate of entropy decrease is much higher than for $R \gtrsim 4.0(a/2)$. For $R \in [3.5(a/2), 4.0(a/2)]$, there is an increase of entropy.

In the cylinder case, the particle volume fraction is lower because of less confinement; i.e., there is less particle absorption into the pore. The two plates case does not show charge separation, and in general, the pressure as a function of R is very different (see Figure 2c). Notice that for $1.5(a/2) < R < 3(a/2)$ the slit pressure is an inward pressure, but this is ruled by the contact pressure component (see Figure 2c and 3c). As a main difference with the more confining geometries, in the slit case, the pressure behavior is ruled by the contact values of the counterion RCPs, at both sides of the plates, and the MST component is of much lower intensity (see Figure 3c).

In Figure 7, $\Delta\sigma_{in}$ and $\Delta\sigma_{out}$ (see eqs 48 and 49) are presented as a function of R for a spherical nanopore. Notice that the loops at $R \approx 3(a/2)$ correspond to that in Figure 2a. $\Delta\sigma_{in} = \Delta\sigma_{out} = 0$ implies that the LEC is satisfied. In contrast to the slit-like pore where LEC is violated at small pore sizes,[26] for spherical and cylindrical geometries, LEC is satisfied only at $R \to \infty$. Apparently, this higher confinement, together with the requirement of constant chemical potential lead to a violation of LEC even for large pores. In spherical geometry, for $R \gtrsim 2.5(a/2)$, the induced charge inside the pore does not compensate the inner

wall charge, whereas for $R \lesssim 2.5(a/2)$ it is overcompensated. At $R \approx 2.5(a/2)$, LEC is satisfied incidentally. For very small pore sizes, almost all the ions (positive and negative) are expelled and $\Delta\sigma_{in}$ decreases again to the limiting value of $-\sigma_0$. If we compare $\bar{\eta}_T^s$ in Figure 6a and $\Delta\sigma_{in}$ in Figure 7, both for $\xi = 6.9$, it is clearly seen that the onset point of the decrease of both curves, at around $R = 4(a/2)$, and the onset point where both curves return to their increasing tendency, at $R \approx 3.5(a/2)$, coincide. In this region, σ'_{in} decreases, implying a decrease in the electrical field and, hence, a decrease in the MST component, as discussed before.

The behavior of the curves for $\Delta\sigma_{in}$ in relation to $\bar{\eta}_i^s$, as a function of R, can be understood as a competition between the need of the system to satisfy electroneutrality inside the pore (eq 36) and the lack of available volume, i.e., as we pointed out above, a competition between the needs of minimizing electrostatic free energy vs maximizing entropy.

IV. Conclusions

We studied the restricted primitive model electrolyte confined by spherical, cylindrical, and slit-like nanopores. Particularly, we have analyzed the pressure, $p(R)$, as a function of the pore size for several cases of divalent electrolyte solutions. In the three geometries, for some fluid conditions, namely subcritical, a van der Waals-like behavior is observed of the pressure of the confined fluid as a function of R; i.e., the isotherms show loops implying a region of negative and positive compressibility, the existence of a critical isotherm, and a spinodal curve. In spherical and cylindrical geometries, an inward pressure is observed $\forall \ R$, whereas for the slit-like pore $p(R)$ has a completely different behavior: $p(R) \rightarrow 0^+$ at intermediate and large values of R, and it oscillates between positive and negative for very small slit widths. In spherical and cylindrical geometries, a charge separation inside the pore is observed; i.e., counterions form a shell next to the pore wall, and coions form a core at the pore center. This phenomenon is not observed in planar geometry. Inward pressure in spherical and cylindrical geometry is driven by the Maxwell stress tensor, which overcomes the contact outward pressure component. The oscillatory behavior of the Maxwell stress tensor occurs for $T < T_c$, which is associated with an increase of counterion concentration at the pore center, i.e., when thermal energy allows ordering of coions. It is pointed out throughout the paper that charge separation is a mechanism with which the system optimizes space and, at the same time, reduces the energy cost of absorbing counterions inside the pore. This is also accompanied by a violation of the local electroneutrality condition. The competition of these two effects, maximizing entropy vs minimizing energy, manifests itself as a van der Waals pressure curve but where the negative compressibility region is real and is explained by the enhancement, due to confinement, of the Maxwell stress tensor inward pressure component.

V. Appendix

A. Derivation of the Pressure Expressions: Contact Theorem for Confined Fluids. The derivation of the pressure expression of the confined fluid was done by a force balance on a fluid element. The electrical field in the fluid is the source of the forces, and its sum is zero because the fluid is in equilibrium; hence

$$\sum_i \mathbf{F}_i = \mathbf{F}(r) + \mathbf{F}(r + dr) + dq\mathbf{E} = 0 \qquad (61)$$

In cylindrical and spherical geometry, the forces have only a radial component. The inner face of the fluid element is at r, whereas the outer face is at $r + dr$. $\mathbf{F}(r)$ and $\mathbf{F}(r + dr)$ are the forces acting on the inner and outer faces, respectively, and are also radial functions. $\mathbf{E}$ is the electrostatic field on the fluid element (Figure 8). Hence, in terms of the electrostatic potential, $E(r) = -(d\Psi(r)/dr)$, dq being the charge inside the volume element dV; it is given by

$$dq = \rho_{el}(r) \, dV = \sum_{i=1}^{2} \rho_{bulk} z_i g_\alpha i(r) \, dV \qquad (62)$$

Therefore, eq 61 as a function of the electrical pressure, $p(r)$, is given as, in the spherical case

$$p(r)(4\pi r^2) - p(r + dr)(4\pi(r + dr)^2) = dqE(r) \quad (63)$$

and in the cylindrical pore

$$p(r)(2\pi Lr) - p(r + dr)(2\pi L(r + dr)) = dqE(r) \quad (64)$$

Using a Taylor expansion, $(p(r + dr) \approx p(r) + (dp(r)/dr)dr + ...)$, we obtain in the spherical geometry

$$2p(r) + r\frac{dp(r)}{dr} = -r\rho_{el}(r)\left(\frac{d\Psi(r)}{dr}\right) \qquad (65)$$

and in the cylindrical case

$$p(r) + r\frac{dp(r)}{dr} = -r\rho_{el}(r)\left(\frac{d\Psi(r)}{dr}\right) \qquad (66)$$

Integrating these equations we obtain, for the spherical case

$$r^2 p(r) - r_0^2 p(r_0) = -\int_{r_0}^{r} y^2 \rho_{el}(y)\left(\frac{d\Psi(y)}{dy}\right) dy \qquad (67)$$

and for the cylindrical pore

$$rp(r) - r_0 p(r_0) = -\int_{r_0}^{r} y \rho_{el}(y)\left(\frac{d\Psi(y)}{dy}\right) dy \qquad (68)$$

By using the relation between the electrostatic potential and $\rho_{el}(r)$, $\rho_{el}(r) = -(\epsilon/4\pi)\nabla^2\Psi(r)$, the previous equations are written as

$$r^2 p(r) - r_0^2 p(r_0) = \frac{\epsilon}{4\pi} \int_{r_0}^{r} y^2 \frac{d\Psi(y)}{dy}\left[\frac{d^2\Psi(y)}{dy^2} + \frac{2}{y}\frac{d\Psi(y)}{dy}\right] dy \qquad (69)$$

for the spherical case, and in the cylindrical pore

$$rp(r) - r_0 p(r_0) = \frac{\epsilon}{4\pi} \int_{r_0}^{r} y \frac{d\Psi(y)}{dy}\left[\frac{d^2\Psi(y)}{dy} + \frac{1}{y}\frac{d\Psi(y)}{dy}\right] dy \qquad (70)$$

Van der Waals-like Isotherms in Confined Electrolyte

J. Phys. Chem. B, Vol. 111, No. 8, 2007 **2043**

Integrating again, the results are, in the spherical geometry

$$r^2 p(r) - r_0^2 p(r_0) = \frac{\epsilon}{8\pi} \int_{r_0}^{r} \left[r^2 \left(\frac{d\Psi(y)}{dy} \right)_r^2 - r_0^2 \left(\frac{d\Psi(y)}{dy} \right)_{r_0}^2 + 2 \int_{r_0}^{r} y \left(\frac{d\Psi(y)}{dy} \right)^2 dy \right] \quad (71)$$

and in the cylindrical case

$$r p(r) - r_0 p(r_0) = \frac{\epsilon}{8\pi} \left[r \left(\frac{d\Psi(y)}{dy} \right)_r^2 - r_0 \left(\frac{d\Psi(y)}{dy} \right)_{r_0}^2 + \int_{r_0}^{r} \left(\frac{d\Psi(y)}{dy} \right)^2 dy \right] \quad (72)$$

These equations are evaluated outside of the pores, with $r = R + d + a/2$ and $r_0 \to \infty$. Far away from the pores, $E(r \to \infty) = -(d\Psi/dr)_{r\to\infty} = 0$ and $p(\infty) = 0$.

In the same way, evaluating inside the pores with $r_0 = 0$ and $r = R - a/2$, $(d\Psi(y)/dy)_0 = 0$ and $p(0) = 0$. Hence, the equations for the pressure outside and inside of spherical shell are

$$p(R + d + a/2) = \frac{\epsilon}{8\pi} \left[E^2(R + d + a/2) + \frac{2}{(R + d + a/2)^2} \int_{\infty}^{R+d+a/2} y E^2(y) \, dy \right] \quad (73)$$

and

$$p(R - a/2) = \frac{\epsilon}{8\pi} \left[E^2(R - a/2) + \frac{2}{(R - a/2)^2} \int_{\infty}^{R+d+a/2} E^2(y) \, dy \right] \quad (74)$$

whereas in the cylindrical pore

$$p(R + d + a/2) = \frac{\epsilon}{8\pi} \left[E^2(R + d + a/2) + \frac{1}{R + d + a/2} \int_{\infty}^{R+d+a/2} E^2(y) \, dy \right] \quad (75)$$

and

$$p(R - a/2) = \frac{\epsilon}{8\pi} \left[E^2(R - a/2) + \frac{1}{R - a/2} \int_{0}^{R-a/2} E^2(y) \, dy \right] \quad (76)$$

Outside the pores, the total pressure on the fluid is $p_T(r) = p(r) + p_{\text{bulk}}$ and using $p_T(R + d + a/2) = k_B T \rho_{\alpha s}(R + d + a/2)$, where $\rho_\alpha s(x) = \sum_{m=1}^{2} \rho_{\text{bulk}} g_{\alpha s}(x)$.

In the same way, inside the pores, $p_T(r) = p(r) + p_0$, where $p_T(R - a/2) = k_B T \rho_{\alpha s}(R - a/2)$. Then, substituting these results in eqs 73−76, the total pressure expressions are, in the spherical case

$$k_B T \rho_{\alpha s}(R + d + a/2) = p_{\text{bulk}} + \frac{\epsilon}{8\pi} \left[E^2(R + d + a/2) + \frac{2}{(R + d + a/2)^2} \int_{\infty}^{R+d+a/2} y E^2(y) \, dy \right] \quad (77)$$

and

$$k_B T \rho_{\alpha s}(R - a/2) = p_0 + \frac{\epsilon}{8\pi} \left[E^2(R - a/2) + \frac{2}{(R - a/2)^2} \int_{0}^{R-a/2} y E^2(y) \, dy \right] \quad (78)$$

whereas in the cylindrical pore

$$k_B T \rho_{\alpha s}(R + d + a/2) = p_{\text{bulk}} + \frac{\epsilon}{8\pi} \left[E^2(R + d + a/2) + \frac{1}{(R + d + a/2)} \int_{\infty}^{R+d+a/2} E^2(y) \, dy \right] \quad (79)$$

and

$$k_B T \rho_{\alpha s}(R - a/2) = p_0 + \frac{\epsilon}{8\pi} \left[E^2(R - a/2) + \frac{1}{(R - a/2)} \int_{0}^{R-a/2} E^2(y) \, dy \right] \quad (80)$$

The pressure difference $p(R)$ is $p_0 - p_{\text{bulk}}$; therefore, using eqs 77−80 for total pressure, the expressions of $p(R)$ given by eqs 39−44 are obtained.

References and Notes

(1) Dabbs, D. M.; Aksay, I. A. *Annu. Rev. Phys. Chem.* **2000**, *51*, 601.
(2) Perottoni, C. A.; da Jornada, J. A. H. *Phys. Rev. Lett.* **1997**, *78*, 2991.
(3) Heuberger, M.; Zach, M.; Spencer, N. D. *Science* **2001**, *292*, 905.
(4) Linhardt, R. J.; Toida, T. *Science* **2002**, *298*, 1441.
(5) Niyogi, S.; Haddon, R. C. *PNAS* **2004**, *101*, 6331.
(6) Jakubek, Z. J.; Simard, B. *Langmuir* **2004**, *20*, 5940.
(7) Jiang, J.; Sandler, S. I.; Smit, B. *Nano Lett.* **2004**, *4*, 241.
(8) Chan, K.-Y.; Tang, Y. W. A.; Szalai, I. *Mol. Simul.* **2004**, *30*, 81.
(9) Baughman, R. H.; Zakhidov, A. A.; de Heer, W. A. *Science* **2002**, *297*, 787.
(10) Austin, R. *Nat. Mater.* **2003**, *2*, 567.
(11) Raviv, U.; Laurat, P.; Klein, J. *Nature* **2001**, *413*, 51.
(12) Yu, J.; Degreve, L.; Lozada-Cassou, M. *Phys. Rev. Lett.* **1997**, *79*, 3656.
(13) Alejandre, J.; Lozada-Cassou, M. *Mol. Phys.* **1996**, *88*, 1317.
(14) Kepler, G. M.; Fraden, S. *Phys. Rev. Lett.* **1994**, *73*, 356.
(15) Goulding, D.; Hansen, J. P.; Melchionna, S. *Phys. Rev. Lett.* **2000**, *85*, 1132.
(16) Allahyarov, E.; D'Amico, I.; Löwen, H. *Phys. Rev. E* **1999**, *60*, 3199.
(17) Nonner, W.; Catacuzzeno, L.; Eisenberg, B. *Biophys. J.* **2000**, *79*, 1976.
(18) Han, Y.; Grier, D. G. *Phys. Rev. Lett.* **2003**, *91*, 038302.
(19) Odriozola, G.; Jiménez-Ángeles, F.; Lozada-Cassou, M. *Phys. Rev. Lett.* **2006**, *97*, 018102.
(20) Bergman, R.; Swenson, J. *Nature* **2000**, *403*, 283.
(21) Koga, K.; Tanaka, H.; Zeng, X. C. *Nature* **2000**, *408*, 564.
(22) Gallo, P.; Rovere, M.; Spohr, E. *J. Chem. Phys.* **2000**, *113*, 11324.
(23) Gulminelli, F.; Chomaz, P. *Phys. Rev. Lett.* **1999**, *82*, 1402.
(24) Argentina, M.; Clerc, M. G.; Soto, R. *Phys. Rev. Lett.* **2002**, *89*, 044301.
(25) Vakarin, E. V.; Duda, Y.; Badiali, J. P. *J. Chem. Phys.* **2006**, *124*, 144515.
(26) Lozada-Cassou, M.; Olivares, W.; Sulbarán, B. *Phys. Rev. E* **1996**, *53*, 522.
(27) Lozada-Cassou, M.; Yu, J. *Phys. Rev. Lett.* **1996**, *77*, 4019.
(28) Kjellander, R.; Marčelja, S.; Pashley, R.-M.; Quirk, J.-P. *J. Chem. Phys.* **1990**, *92*, 4399.
(29) Kjellander, R.; Åkesson, T.; Jönsson, B.; Marčelja, S. *J. Chem. Phys.* **1992**, *97*, 1424.
(30) Evans, R. *J. Phys. Cond. Matt.* **1990**, *2*, 8989.
(31) Boda, D.; Busath, D. D.; Henderson, D.; Sokolowski, S. *J. Phys. Chem.* **2000**, *104*, 8903.
(32) Yeomans, L.; Feller, S. E.; Sánchez-Arellano, E.; Lozada-Cassou, M. *J. Chem. Phys.* **1993**, *98*, 1436.
(33) Lozada-Cassou, M.; Yu, J. *Phys. Rev. E* **1997**, *56*, 2958.
(34) Lozada-Cassou, M.; Olivares, W.; Sulbarán, B.; Yu, J. *Physica A* **1996**, *231*, 197.
(35) Deserno, M.; Jiménez-Ángeles, F.; Holm, C.; Lozada-Cassou, M. *J. Phys. Chem. B* **2001**, *105*, 10983.
(36) Jiménez-Ángeles, F.; Lozada-Cassou, M. *J. Phys. Chem. B* **2004**, *108*, 1719.
(37) Jiménez-Ángeles, F.; Lozada-Cassou, M. *J. Phys. Chem. B* **2004**, *108*, 7286.
(38) Lozada-Cassou, M.; Saavedra-Barrera, R.; Henderson, D. *J. Chem. Phys.* **1982**, *77*, 1550.
(39) y Terán, L. M.; Suh, S. H.; White, H. S.; Davis, H. T. *J. Chem. Phys.* **1990**, *92*, 5087.

(40) Torrie, G.; Valleau, J. *J. Chem. Phys.* **1980**, *73*, 5807.

(41) Torrie, G.; Valleau, J. *J. Phys. Chem.* **1982**, *86,* 3251.

(42) Messina, R.; Holm, C.; Kremer, K. *Phys. Rev. Lett.* **2000**, *85,* 872.

(43) Degreve, L.; Lozada-Cassou, M.; Sánchez, E.; González-Tovar, E. *J. Chem. Phys.* **1993**, *98*, 8905.

(44) Wang, K.; Yu, Y.-X.; Gao, G.-H.; Luo, G.-S. *J. Chem. Phys.* **2005**, *123*, 234904.

(45) González-Tovar, E.; Jiménez-Ángeles, F.; Messina, R.; Lozada-Cassou, M. *J. Chem. Phys.* **2004**, *120*, 9782.

(46) Degreve, L.; Lozada-Cassou, M. *Phys. Rev. E* **1998**, *57*, 2978.

(47) Lozada-Cassou, M. *J. Chem. Phys.* **1981**, *75*, 1412.

(48) Lozada-Cassou, M. In *Fundamentals of Inhomogeneus Fluids*; Henderson, D., Ed.; Marcel Dekker: New York, 1992; Chapter 8.

(49) Waisman, E.; Lebowitz, J. L. *J. Chem. Phys.* **1972**, *56*, 3086.

(50) Waisman, E.; Lebowitz, J. L. *J. Chem. Phys.* **1972**, *56*, 3093.

(51) González-Tovar, E.; Lozada-Cassou, M. *J. Phys. Chem.* **1989**, *93*, 3761.

(52) Lozada-Cassou, M. *J. Chem. Phys.* **1984**, *80*, 3344.

(53) Lozada-Cassou, M.; Díaz-Herrera, E. *J. Chem. Phys.* **1990**, *92*, 1194.

(54) González-Tovar, E.; Lozada-Cassou, M.; y Terán, L. M. *J. Chem. Phys.* **1991**, *95*, 6784.